Geophysical Research Letters

RESEARCH LETTER
10.1029/2024GL109171

Key Points:

- We examine the spatial and temporal evolution of near-source material properties during the 2019 Ridgecrest earthquake sequence
- The spatially homogeneous V_p/V_s ratios in the rupture zones indicate little structural resistance during the earthquake ruptures
- The temporal changes in V_p/V_s ratios suggest fluid presence, which may have facilitated the nucleation of the 2019 Ridgecrest mainshock

Supporting Information:

Supporting Information may be found in the online version of this article.

Correspondence to:

G. Lin,
glin@miami.edu

Citation:

Lin, G., & Fan, W. (2024). Spatiotemporal variations of in situ V_p/V_s ratios during the 2019 Ridgecrest earthquake sequence suggest fault zone condition changes. *Geophysical Research Letters*, *51*, e2024GL109171. https://doi.org/10.1029/2024GL109171

Received 8 MAR 2024
Accepted 14 APR 2024

Spatiotemporal Variations of In Situ V_p/V_s Ratios During the 2019 Ridgecrest Earthquake Sequence Suggest Fault Zone Condition Changes

Guoqing Lin[1] **and Wenyuan Fan**[2]

[1]Rosenstiel School of Marine, Atmospheric, and Earth Science, University of Miami, Miami, FL, USA, [2]Scripps Institution of Oceanography, University of California, San Diego, CA, USA

Abstract The 2019 Mw 7.1 Ridgecrest earthquake was the largest event in California over the past 20 years. The earthquake was preceded by a sequence of foreshocks. However, the physical processes leading to the mainshock remain unclear. Here, we image the ratios of compressional (P)- to shear (S)-wave velocity (V_p/V_s) in the fault zones and examine the spatial and temporal evolution of near-source material properties during the Ridgecrest earthquake sequence. We find that the V_p/V_s ratios are spatially homogeneous in the rupture zones, indicating a lack of fault-zone material difference along strike. We identify an anomalously low V_p/V_s ratio fault patch near the mainshock hypocenter before its occurrence, which returned to the background value after the earthquake. This low V_p/V_s ratio suggests fluid overpressure, which may have facilitated the nucleation of the 2019 Ridgecrest mainshock.

Plain Language Summary Understanding the earthquake nucleation process has direct implications for earthquake physics and seismic hazards. Specifically, identifying the geophysical processes within fault zones that precede and result in subsequent earthquakes has been of great interest to the earthquake science community. This study explores how the ratio of compressional (P) wave speed to shear (S) wave speed changes in both space and time and their correlations with the subsequent seismicity evolution, focusing on the 2019 Ridgecrest earthquake sequence in California. In most slipping areas of the earthquakes, the P-wave to S-wave speed ratios are relatively uniform. However, in places where faults end, cross each other, or change direction, we observe unusual values. We find high ratios near the three major earthquakes on a small scale. Additionally, the ratios change where the main earthquake (magnitude 7.1) initiated. The ratios are low between a moderate (magnitude 5.4) and the main (magnitude 7.1) earthquake and increase after the main earthquake, indicating the presence of over-pressurized fluids near the earthquake source. The associated high pore pressure might have helped nucleate the Ridgecrest mainshock. Our findings show that these speed ratios can be highly sensitive to seismic activities and could help us better understand how earthquakes start.

1. Introduction

The 2019 Ridgecrest earthquake sequence comprises the most significant earthquakes in California for the past 20 years. On 4 July 2019, a moment magnitude (Mw) 6.4 earthquake struck approximately 13 km southwest of Searles Valley, California (Ross et al., 2019). Nearly 34 hr later, an Mw 7.1 earthquake ruptured a complex fault system extending over 75 km to the northwest direction. This event marks the largest earthquake in southern California since the 1992 Mw 7.3 Landers and the 1999 Mw 7.1 Hector Mine earthquakes. Approximately 2,500 aftershocks occurred in between the Mw 6.4 foreshock and the Mw 7.1 mainshock, including an Mw 5.4 earthquake about 4 hr before and 2.4 km southeast of the mainshock (Hauksson & Jones, 2020). The Ridgecrest earthquakes ruptured multiple segments of the fault system, including non-vertical, interlaced orthogonal conjugate faults (Lin, 2020; Shelly, 2020). The close spatiotemporal correlation between the foreshocks and the mainshock suggest a causal triggering relationship. However, the foreshocks did not instantaneously trigger the Mw 7.1 mainshock, and there is an approximately 34 hr delay between the Mw 6.4 foreshock and the mainshock.

The static or dynamic stress perturbation from the Mw 6.4 foreshock appear to be insufficient to trigger the mainshock rupture (Jin & Fialko, 2020; Lozos & Harris, 2020; Taufiqurrahman et al., 2023), suggesting that additional fault zone processes might have helped nucleate the Mw 7.1 mainshock. Foreshocks are often the most accessible observations for inferring mainshock nucleation processes, which are likely due to stress interactions that eventually lead to the triggering of mainshocks (Abercrombie & Mori, 1996; Kato et al., 2012; Ruiz

et al., 2014). For example, accelerating aseismic slip events have been hypothesized to nucleate subsequent earthquakes and can also produce foreshocks as by-products during their propagation (Ellsworth & Beroza, 1995). Foreshocks may also result from a sequence of stress-triggering events among themselves, eventually cascading into a larger event known as the mainshock (Ide, 2019; McLaskey, 2019; Meng & Fan, 2021). Direct laboratory observations of multi-scale damage evolution in the failure zone (fault zone) reveal the interplay between various deformation mechanisms; and their competing effects determine the path to macroscopic failures (Renard et al., 2017, 2018). Such experiments suggest that fault nucleation and propagation processes exist; however, their evolution depends not only on the states of fault stress but also, more importantly, on the strength conditions of the fault zone, which can evolve rapidly near the earthquake hypocenters. Therefore, resolving the material properties and conditions of the fault zone at the scales of earthquake nucleation is critical for understanding the evolution of the Ridgecrest earthquake sequence.

The ratio of compressional (P)- to shear (S)-wave velocity (V_p/V_s) is sensitive to both fault strength and stress state due to its direct connection with Poisson's ratio, fluid content, and pore fluid pressure (e.g., Brantut & David, 2019; Christensen, 1996; Takei, 2002). In fault systems, V_p/V_s ratios reflect the composition of rocks, the presence of cracks, and the degree of pore fluid saturation (Lin et al., 2022; Liu et al., 2023), all of which directly control earthquake sequences (e.g., Zhu et al., 2020). However, resolving V_p/V_s ratios at seismogenic depths, where great earthquakes occur, is challenging. Seismic tomography can image V_p/V_s ratios at depth, but conventional passive imaging techniques are strongly influenced by seismic wave propagation. As a result, these models may be overly smooth when compared to the dimensions of most earthquake ruptures (Tong et al., 2021; Yang et al., 2022). Furthermore, tomographic models often lack the temporal resolution needed to detect rapid spatiotemporal variations that occur during the earthquake preparation stages. In this study, we apply a high-resolution estimation method that uses waveform cross-correlation data to calculate in situ V_p/V_s ratios in the near-source regions of the 2019 Ridgecrest earthquake sequence. We directly resolve fault-zone material properties, complementing existing velocity structure models. Additionally, we synthesize a collection of geophysical evidence to evaluate the faulting environments and discuss the possible physical causes of the Ridgecrest earthquake sequence.

2. Data

We use over 164 million *P*- and *S*-wave differential times, along with the corresponding correlation coefficients, from 1 million event pairs to resolve the in situ V_p/V_s ratios in the fault zones of the 2019 Ridgecrest earthquake sequence. These waveform cross-correlations and differential times originate from 24,925 relocated earthquakes that occurred between 1 January and 31 August 2019 (Figure 1a; Lin, 2020). The catalog is accurate in both absolute and relative locations, obtained using ray tracing through a three-dimensional (3-D) seismic velocity model (Zhang & Lin, 2014) and a waveform cross-correlation relocation technique (Lin, 2018; Lin & Shearer, 2006).

3. Methodology

The high-resolution V_p/V_s ratio estimation method uses differential times from waveform cross-correlation to study spatial and temporal variations of near-source V_p/V_s ratios in different tectonic regions (Lin & Shearer, 2007). For a compact cluster of events, the waveforms for each pair of events observed at the same station will be similar enough so that the cross-correlation can be computed. This method assumes that the scale length of changes in the V_p/V_s ratio is greater than the size of the similar event clusters so that the V_p/V_s ratio can be treated as a constant within the event cluster. The best-fitting V_p/V_s ratio for the entire cluster can be obtained by fitting all the points of the demeaned differential *P*- and *S*-arrival times simultaneously. A hybrid L_1–L_2 fitting method is adopted for the procedure (Lin & Shearer, 2007), which is more robust to outliers in the observations than the traditional least squares fitting.

The most accurate V_p/V_s results for real data can be obtained for clusters with a three-dimensional distribution of events (Lin & Shearer, 2007). In order to estimate the spatial distribution of events in each cluster, we use the method of principal component analysis (e.g., Kirschvink, 1980) to compute eigenvalues for the covariance matrix of the earthquake locations for all similar event clusters. Clusters are considered to have nearly spherical distribution if $\lambda_1/\lambda_3 \leq K$, where eigenvalues $\lambda_1 \geq \lambda_2 \geq \lambda_3$, and K is a constant (Lin & Shearer, 2009; Michelini & Bolt, 1986; Shearer et al., 2003). Standard errors in the V_p/V_s estimates are calculated by applying a bootstrap

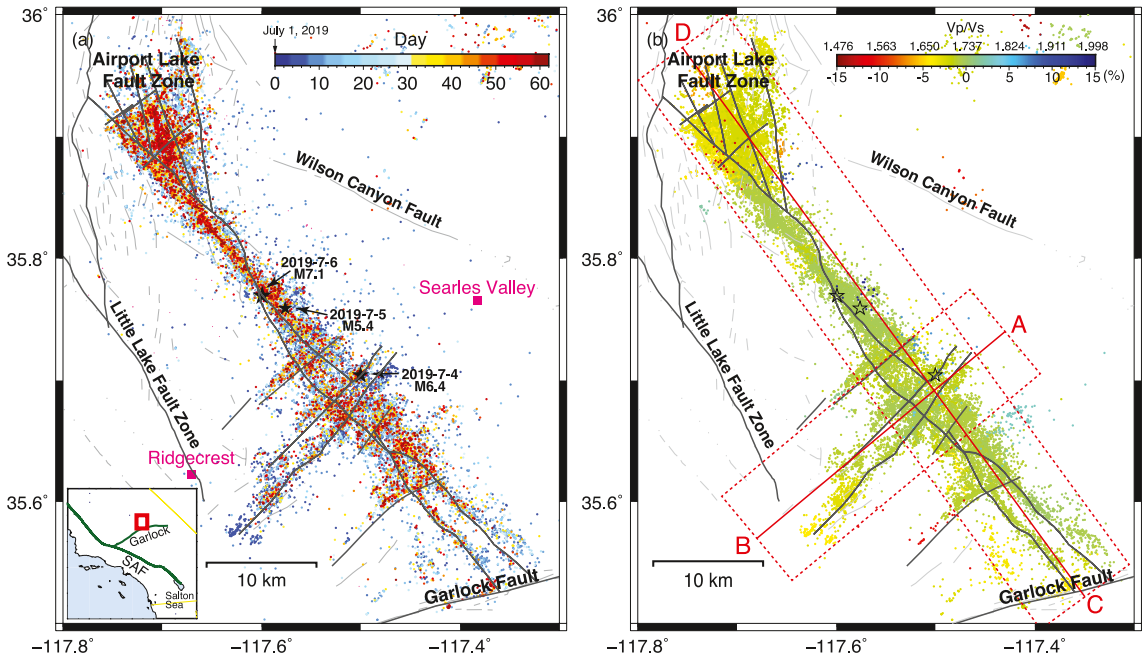

Figure 1. (a) Map view of the waveform cross-correlation relocations by Lin (2020) for the first 8 months of 2019 in the adjacent area of the Ridgecrest earthquake sequence. Pink dots represent the background seismicity before 1 July 2019. Events from July 1 to August 31 are colored by days since 1 July 2019. Stars mark the Mw 6.4, 5.4, and 7.1 earthquakes on July 4, 5, and 6 2019 (UTC). The inset map shows the location of the study area in California. (b) Map view of the earthquakes in the similar event clusters with robust V_p/V_s ratios. Events are colored by the corresponding in situ V_p/V_s ratio. The red straight lines (A–B and C–D) and dotted boxes are the profiles and boundaries for the cross-sections in the following figures.

approach (Efron & Gong, 1983; Efron & Tibshirani, 1991), in which each pair of suitable differential P and S times in the same cluster may be sampled multiple times or not sampled at all. This process is repeated for many subsamples for each cluster and the standard deviation of these subsamples is used as the standard error of the V_p/V_s ratio. In this study, we use differential times with a waveform correlation coefficient of 0.6 or greater in the calculation and require each event pair have at least eight individual differential times with correlation coefficients of 0.65 or greater. Furthermore, we select the clusters with $\lambda_1/\lambda_3 \leq 25 = K$ and discard V_p/V_s ratios with the estimated standard errors greater than 0.03. The standard errors are computed from 100 bootstrap resamples.

4. Results and Discussion

The V_p/V_s estimates are most sensitive to materials near the earthquake sources; complex wave propagation effects due to surrounding 3-D seismic structures have minimal impact on the results (Lin & Shearer, 2007; Liu et al., 2023). Theoretically, the resolution can be as high as the spatial and temporal inter-event separation. In this study, we first cluster the earthquakes and apply a sequence of quality control steps before estimating V_p/V_s ratios to ensure their robustness (see Figures S1 and S2 in Supporting Information S1). As a result, we identify 80 similar event clusters satisfying our selection criteria, comprising a total of 24,082 events. The sizes of these clusters range from 10 to 1,356 events, and they are nearly uniformly distributed across the Ridgecrest fault system. These clusters are centered at depths ranging from the surface to 19 km, and the majority of average inter-event distances are less than 3 km. The in situ V_p/V_s ratios for the 80 clusters are estimated in the range of 1.51–1.97 (Figures 1b, 2a, and 2b). Example plots of the demeaned differential times are shown for two clusters (see Figure S3 in Supporting Information S1).

4.1. Comparison With Tomographic Velocity Model

For comparison, we interpolate the 3-D tomographic models by Zhang and Lin (2014) (Figure S4 in Supporting Information S1) at the earthquake locations to extract both V_p and V_p/V_s values. We then calculate the average V_p and V_p/V_s value in each cluster and compare these average values with our in situ V_p/V_s ratios (Figures 2c–2f). The average velocity values from all the seismicity along profiles A–B and C–D, 1.737 for V_p/V_s and 5.962 km/s

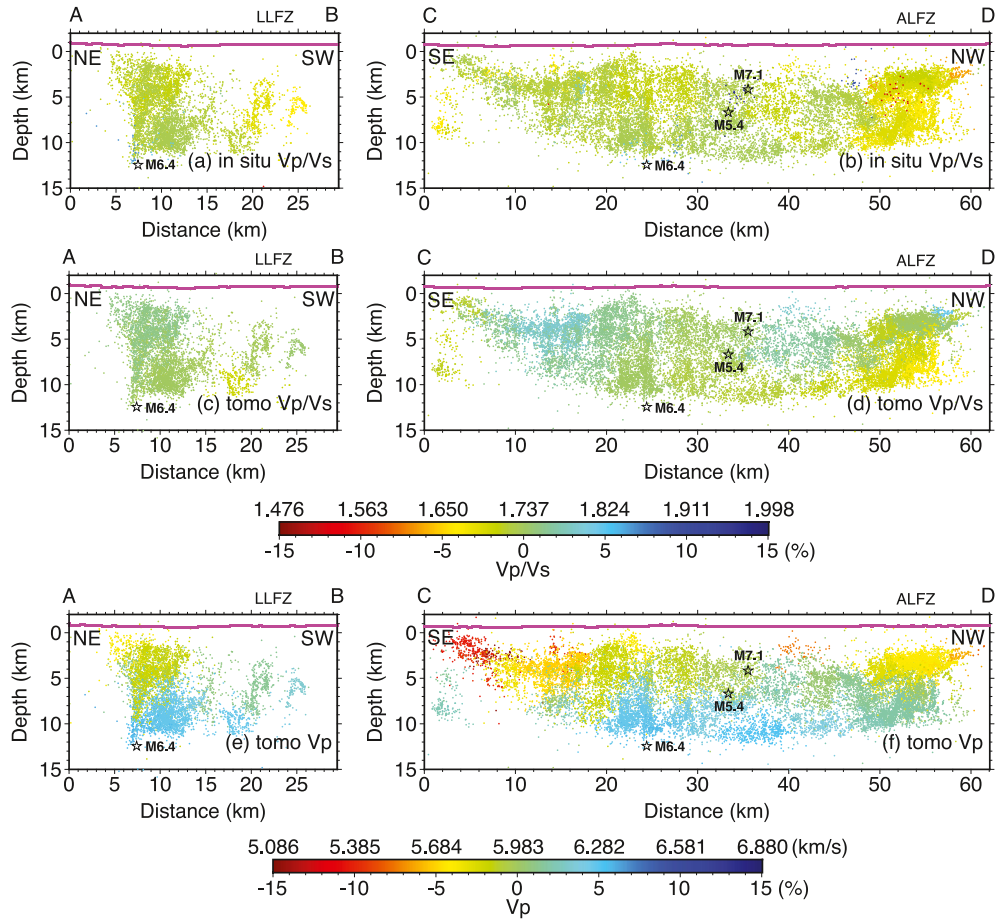

Figure 2. (a), (b) Depth distribution of seismicity, colored by the in situ V_p/V_s ratio for the corresponding cluster, along profile A–B and C–D and enclosed by the corresponding dotted box in Figure 1b, respectively. (c), (d) Tomographic V_p/V_s and (e), (f) tomographic V_p values for events in the similar earthquake clusters along the two profiles. Events are colored by the average velocity value for each cluster. Stars represent the 3-D relocations of the Mw 6.4, 5.4, and 7.1 earthquakes by Lin (2020). The purple lines at the top of the cross sections show the local topography. Zero depth refers to mean sea level. Abbreviations are LLFZ, Little Lake Fault Zone; and ALFZ, Airport Lake Fault Zone.

for V_p, are used as the references for the percentage plots. Both the tomographic V_p/V_s (Figures 2c and 2d) and V_p (Figures 2e and 2f) models are more spatially heterogeneous than the in situ V_p/V_s ratios in the Ridgecrest fault zones, suggesting material variations from one segment to another. The tomographic V_p/V_s model (Figures 2c and 2d) have values varying from 1.69 to 1.76, which are generally higher than the in situ results. The only exception occurs near the Airport Lake Fault Zone (ALFZ) (50–60 km distance, below 5 km depth in Figure 2c), where the tomographic V_p/V_s model has lower ratios of ~1.66. The tomographic V_p model (Figures 2e and 2f) shows great variations along the two profiles with increasing V_p values with depth, a pattern which is absent in either the tomographic and in situ V_p/V_s ratios.

The tomographic V_p model suggests significant material variability along the fault strike, which may be related to the complex tectonics of the Eastern California Shear Zone (ECSZ; Dokka & Travis, 1990). However, such complexities are not observed in our in situ V_p/V_s results. The differences between the in situ V_p/V_s ratios and the tomographic models may primarily stem from the contrast between the seismic structures surrounding the fault zone and the fault zone material properties themselves (Qiu et al., 2021; Tong et al., 2021; White et al., 2021; Yang et al., 2022). These observed differences suggest that although the Ridgecrest fault system is situated in the complex ECSZ and surrounded by host rocks with strong variations, the fault zones themselves are relatively homogeneous. This is different from the fault zone material segmentation observed in other strike-slip fault systems (Lin et al., 2022; Liu et al., 2023). For example, the westernmost Gofar transform fault, an analogous site to the Ridgecrest fault system, a barrier zone associated with anomalous V_p/V_s have repeatedly stopped adjacent

M6 earthquakes to rupture further (Gong & Fan, 2022; Liu et al., 2023; McGuire et al., 2012). This barrier zone is likely highly damaged with active seawater infiltration, causing material and fault condition contrasts (Kohli et al., 2021; Roland et al., 2012).

The differences between the in situ and tomographic results are likely due to the data sets, inversion techniques, and varying sensitivities to different spatial scales. The tomographic models are constructed using 30 years of body wave travel-time data (Zhang & Lin, 2014) and they represent both the spatial and temporal average of the velocity structures in the study area. In contrast, the in situ V_p/V_s estimates are obtained using the 2 months aftershock data and are most sensitive to the fault zone structures. In the tomographic inversion, velocity perturbations, instead of absolute values, are solved relative to the initial model, showing strong dependence on the starting values (e.g., Lin et al., 2007, 2010, 2014, 2021; Zhang & Lin, 2014). The in situ V_p/V_s estimation method is based on a robust least squares linear fitting and does not rely on the initial value (Lin & Shearer, 2007). In addition, tomographic models are dependent on inversion parameters, such as damping and smoothing factors. Tomographic V_p/V_s inversions also limit the model perturbations to improve inversion stability and convergence.

4.2. Homogeneous Fault Zone Materials Facilitating Earthquake Rupture Propagation

The Ridgecrest fault zones exhibit relative homogeneity in V_p/V_s ratios (1.71–1.73, Figure 1b, 3–19 km distance in Figure 2a and 3–46 km distance in Figure 2b), particularly where the majority of slip occurred during the Mw 6.4 foreshock and the Mw 7.1 mainshock (Jin & Fialko, 2020; Ross et al., 2019). The Mw 6.4 foreshock was dominated by slip on a northeast-trending, left-lateral fault (Jia et al., 2020; Wang et al., 2020b), where the slip propagated toward the Little Lake Fault Zone (LLFZ, 20–26 km distance in Figure 2a). We find that its rupture arresting boundary correlates with lower V_p/V_s ratios (1.66–1.69) at the southwestern end of the LLFZ. Similarly, we observe lower V_p/V_s ratios near the Garlock fault (GF, ∼3 km distance in Figure 2b) and in the ALFZ (46–60 km distance in Figure 2b) along the northwest-trending, right-lateral fault where the Mw 7.1 mainshock halted its rupture propagation (Jia et al., 2020; Wang et al., 2020b). Similar to Lin et al. (2022), we identify anomalous V_p/V_s ratios in areas where fault segments intersect, terminate, or change orientations (e.g., ALFZ), where the ratios range from 1.52 to 1.89. Intriguingly, the areas surrounding the hypocenters of both the Mw 6.4 and Mw 7.1 earthquakes have sporadic clusters with relatively high V_p/V_s ratios, peaking at a value of 1.97 for one cluster near the Mw 7.1 mainshock's hypocenter (33–36 km distance in Figure 2b). Similar high V_p/V_s ratios are also observed near the Mw 5.4 earthquake, albeit with subdued variations. These clusters include earthquakes that occurred both before and after the three major earthquakes, and the anomalous values likely associate with the changes of the fault environment due to the earthquakes (Trugman et al., 2020). The overall homogeneous V_p/V_s ratio distribution in the Ridgecrest fault system distinctly differs from those observed in the Parkfield segment of the San Andreas Fault in Northern California, as well as the San Jacinto Fault Zone and its adjacent regions in Southern California (Lin et al., 2022).

The homogeneous material within the fault zone may suggest relatively homogeneous fault conditions, and the lack of material segmentation may have encouraged the earthquake rupture propagation, thereby facilitating the development of both the Mw 6.4 foreshock and the Mw 7.1 mainshock (Wibberley et al., 2008). The 2019 earthquake sequence ruptured numerous immature and largely unmapped faults, which were not previously recognized as a connected system capable of hosting major earthquakes (Ponti et al., 2020). The earthquake sequence cascaded across hierarchically interlaced, antithetic faults (Ross et al., 2019), which are likely statically strong (Fialko, 2021; Fialko & Jin, 2021). These geological and structural complexities seem to likely inhibit the rupture propagation across the entire fault system. Therefore, various weakening mechanisms might have played critical roles in facilitating the observed rupture propagation (Milliner et al., 2022; Taufiqurrahman et al., 2023). As shown in our in situ V_p/V_s ratios, the Ridgecrest fault zones are surprisingly homogeneous. This structural simplicity may have facilitated rupture propagation due to a lack of seismic structural barriers (McGuire et al., 2012), specifically on the northwest-trending fault where the mainshock occurred (Figure 2b). Variations in the resolved V_p/V_s ratios near the edges of the fault zones indicate transitions in material properties and fault zone environments, which may have contributed to arresting the foreshock and mainshock rupture propagation (Wibberley et al., 2008), in addition to the effects of prestress-to-strength distribution in the fault zones (Taufiqurrahman et al., 2023).

Table 1
Details of the Seismicity Sequences in Different Time Periods

	ALL	BEFORE	MIDDLE1	MIDDLE2	AFTER
Time Span	Jan 1–Aug 31	Jan 1–Mw 6.4	Mw 6.4–Mw 5.4	Mw 5.4–Mw 7.1	Mw 7.1–Aug 31
No. of EQKs	24,082	0	626	695	22,361
No. of clusters	80	0	10	11	74

Note. ALL: all the earthquakes from 1 January to 31 August 2019; BEFORE: events before the Mw 6.4 earthquake on July 4; MIDDLE1: events between the Mw 6.4 and 5.4 earthquakes; MIDDLE2: events between the Mw 5.4 and 7.1 earthquakes; and AFTER: earthquakes after the Mw 7.1 mainshock on July 6. Note that we only show information for clusters with robust V_p/V_s ratios.

4.3. Theoretical Crack Models

In order to understand the observed V_p/V_s anomalies, we explore the effects of porosity and aspect ratio on in situ V_p/V_s ratios by applying the Kuster-Toksöz theoretical crack model (Kuster & Toksöz, 1974). The Kuster-Toksöz elastic wave-scattering method appears to be more accurate than some of the self-consistent approaches, even though it does not explicitly consider inclusion interactions (Zimmerman, 1984). We construct idealized porous-medium models with different inclusions in ellipsoidal shapes and assume an over-pressurized condition to compare our observed in situ V_p/V_s ratios with theoretical predictions. We use V_p of 5.962 km/s and V_p/V_s ratio of 1.737 from the tomographic model as the background values for the host rock. Because of the presence of large number of carbonate fragments in the area (Thompson Jobe et al., 2020), we examine water and carbon dioxide (CO_2) inclusions for our theoretical modeling (Figure S5 in Supporting Information S1) and assume water velocity and density as $V_p = 1.5$ km s^{-1} and $\rho = 1.0$ Mg m^3 and CO_2 velocity and density as $V_p = 0.4$ km s^{-1} and $\rho = 0.75$ Mg m^3 (Adam & Otheim, 2013; Lemmon et al., 2023; Takei, 2002). The ellipsoidal crack shapes are evaluated with their aspect ratios ranging from 0.001 to 0.3. For water-filled cracks, V_p reduces with increased porosity, however, V_p/V_s can either increase or decrease, depending on aspect ratio. For very flat water-filled cracks (aspect ratio $\leq$0.01), the V_p/V_s ratio increases with porosity; whereas for more spherical cracks, V_p/V_s decreases with porosity. Including CO_2 would reduce both the V_p and V_p/V_s, regardless of aspect ratio. Similar results are yielded by applying Walsh (1969) or O'Connell and Budiansky (1974) approaches. Our idealized modeling can help explain the correlations between the tomographic V_p and in situ V_p/V_s ratio, although interpreting their absolute values require adopting more sophisticated models (e.g., Brantut & David, 2019). The model suggests a positive correlation between the tomographic V_p and in situ V_p/V_s ratio if CO_2 and/or more spherical water-filled cracks are involved. In contrast, a negative correlation is expected if flat water-filled cracks exist. It is important to note that the presence of water is often associated with high V_p/V_s ratios as a result of water reducing the shear modulus. This leads to decreases in both V_p and V_s, but with a greater effect on V_s, resulting in a high V_p/V_s ratio, showing as a negative correlation. This correlation is commonly used to interpret the low V_p and high V_p/V_s ratio as the existence of fluids in tomographic models. However, laboratory experiments (Christensen, 1996; Takei, 2002) and our crack model demonstrate that water inclusions can either increase or decrease the V_p/V_s ratio (Figure S5b in Supporting Information S1), depending on crack porosity and geometry. According to the crack model, thick cracks (i.e., large aspect ratios) can lower V_p/V_s ratios, while thin cracks are more likely to result in high V_p/V_s ratios. We notice that the aspect ratio and porosity cannot reduce the V_p/V_s ratio to below 1.5 if only water inclusions are considered. This suggests that another type of inclusion might have been present, leading to the low value of 1.45 observed in this study, such as CO_2 only or a combination of water and CO_2.

4.4. Imaging Fault Zone Environments in Space and Time

The abundant seismicity of the Ridgecrest earthquake sequence offers a rare opportunity to examine short-term changes of in situ V_p/V_s ratios. We segment the earthquake sequences into four time periods, using the timings of the Mw 6.4 and Mw 5.4 foreshocks and the Mw 7.1 mainshock as delineation points. These periods are termed "BEFORE," "MIDDLE1," "MIDDLE2," and "AFTER" (Table 1 and Figures 3 and 4). There are few earthquakes before the Mw 6.4 foreshock to form reliable clusters. We conduct separate earthquake cluster analyses for each period and then estimate the in situ V_p/V_s ratios for event clusters within each period. We use the same parameters and selection criteria for V_p/V_s estimation as for the entire data set (Table 1). We find that the V_p/V_s ratios near the Mw 7.1 mainshock increased from 1.45 to 1.72 between the "MIDDLE2" and "AFTER" periods (see Figure S3 in

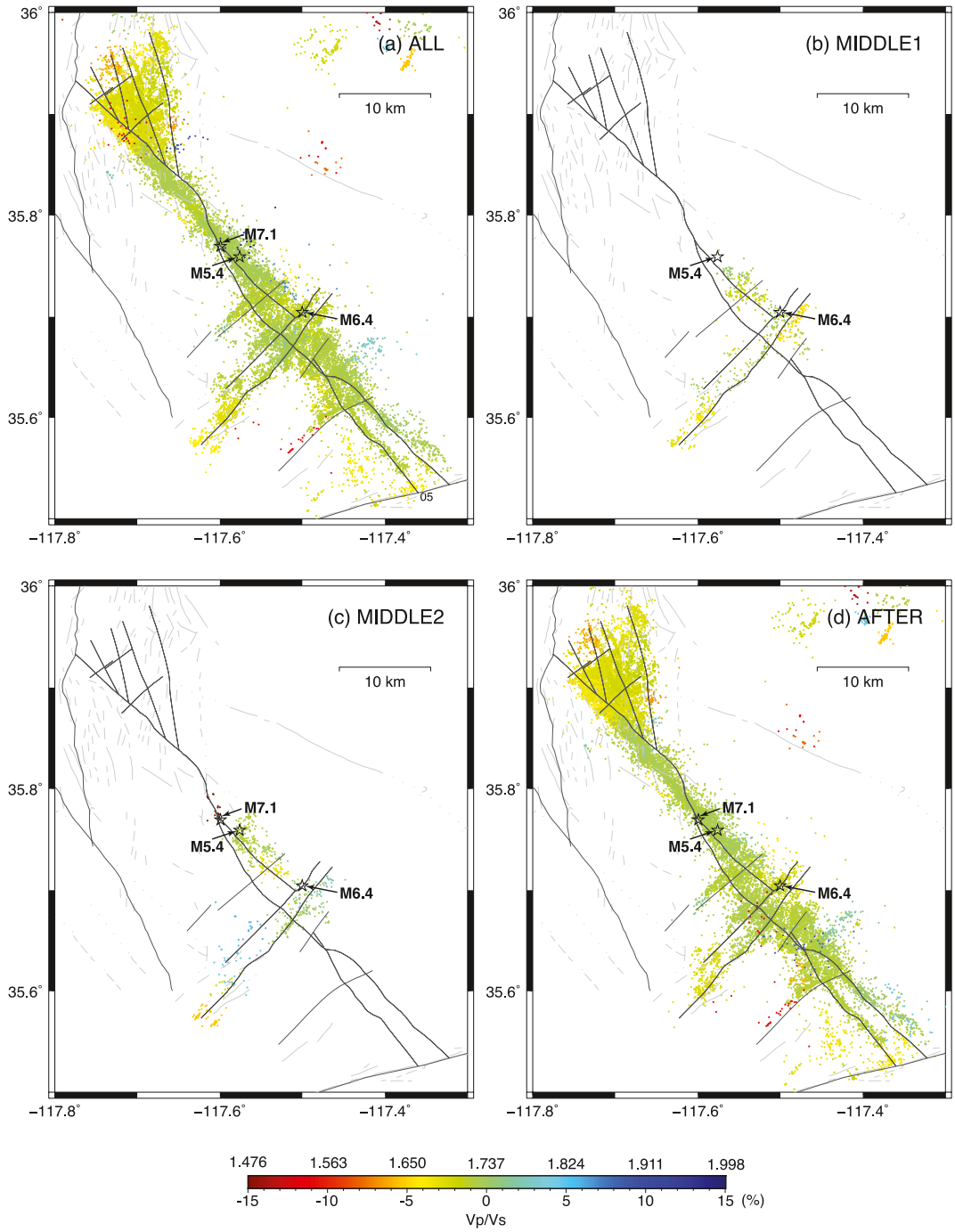

Figure 3. Map views of earthquakes in the similar event clusters for different time periods, colored by the in situ V_p/V_s ratio for each cluster. ALL: 1/1/2019 ~ 8/31/2019; MIDDLE1: 7/4/2019 ~ 7/5/2019; MIDDLE2: 7/5/2019 ~ 7/6/2019; and AFTER: 7/6/2019 ~ 8/31/2019. "BEFORE" is not shown here because there are no robustly resolved clusters in this period.

Supporting Information S1 for best-fitting V_p/V_s ratios), suggesting an abrupt change in the fault zone environment near its hypocenter (Figures 3c and 3d). From "MIDDLE1" to "MIDDLE2", the V_p/V_s ratios all increased for the clusters located above the Mw 6.4 foreshock, whereas those near the Mw 5.4 and Mw 7.1 earthquakes all decreased (Figures 3 and 4). We also observe a high V_p/V_s ratio of 1.97 for a nearby cluster in the entire data set (Figure 4a2), in which only one earthquake occurred 3 hr before the mainshock and the rest after it. The differences in the values between the "MIDDLE2" and entire data set suggest a possible structural change or

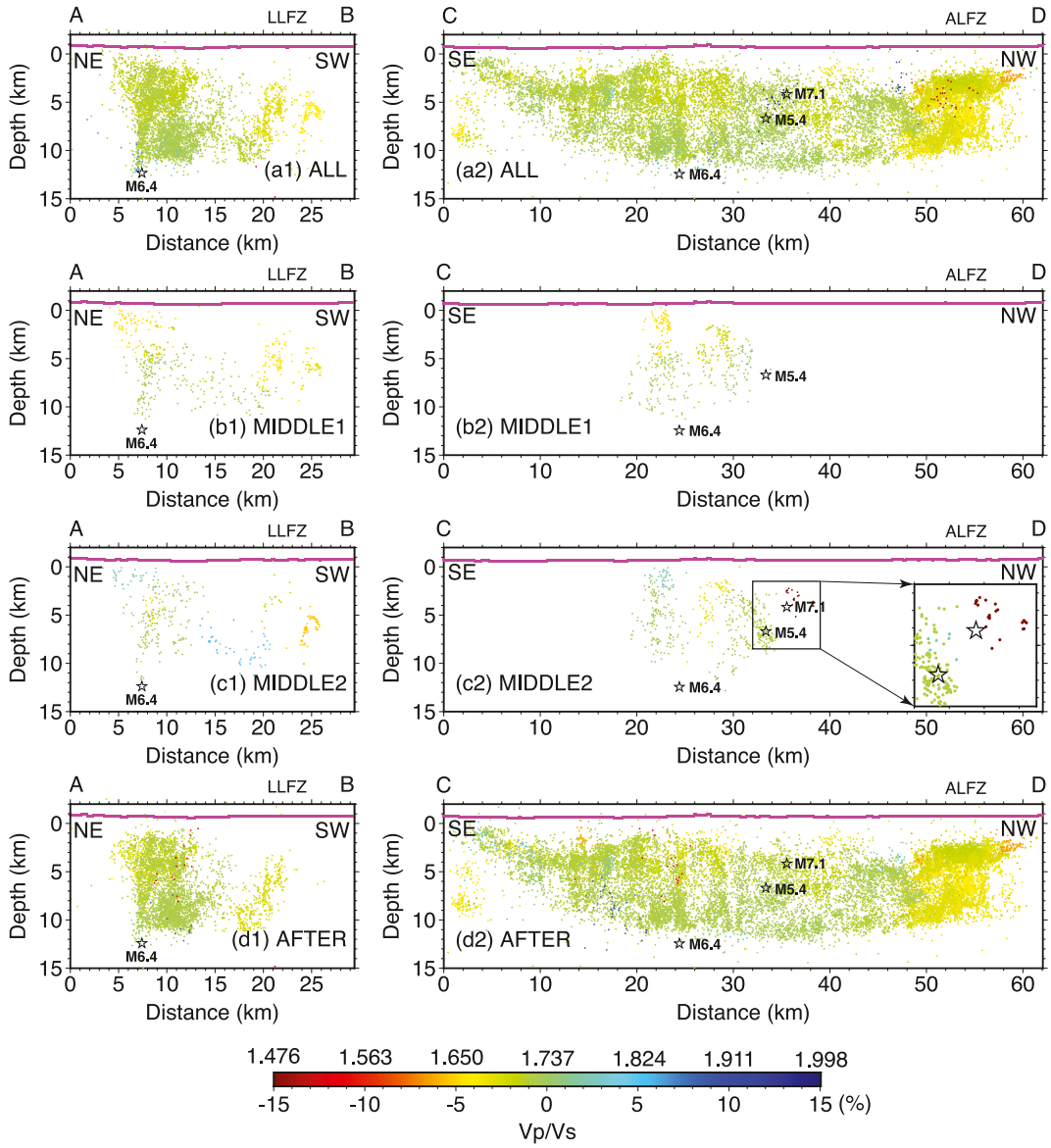

Figure 4. Depth distributions of seismicity along profiles A–B (a1–d1) and C–D (a2–d2) for different time periods. Symbols are the same as those in Figure 2.

reactivation caused by the earthquake. The aftershocks in the nearby cluster from the entire data set are grouped into a bigger cluster in "AFTER" (Figure 3d) with a normal V_p/V_s value of 1.72. This indicates that if the cluster size is too big, the average V_p/V_s will be captured over a relatively large spatial scale and any small-scale variations may be missed (see Supporting Information S1).

4.5. Changes in Fault Environment Near the 2019 M7.1 Ridgecrest Earthquake Hypocenter

We identify a transient change in the in situ V_p/V_s ratio at the hypocenter of the Mw 7.1 mainshock, which increased from 1.45 to 1.72 before and after the earthquake (Figure 3). Prior to the Mw 6.4 foreshock, the Ridgecrest fault system is seismically quiescent. Between the Mw 6.4 and Mw 5.4 foreshocks, seismicity forms an L-shaped distribution in the fault zones without extending beyond the location of the Mw 5.4 foreshock (Hauksson & Jones, 2020). During this period and the subsequent time between the Mw 5.4 and Mw 7.1 earthquakes, the in situ V_p/V_s ratios maintain a nominal value around 1.70–1.74 for the same fault segment (Figures 3b and 3c). Intriguingly, V_p/V_s ratios appear to increase for the clusters located around the connection of

the northeast-trending and northwest-trending faults from "MIDDLE1" to "MIDDLE2." In contrast, V_p/V_s ratios near the Mw 5.4 and Mw 7.1 hypocenters seem to decrease during these periods (Figure 4). Moreover, a low V_p/V_s ratio patch of 1.45 exists near the Mw 7.1 mainshock during "MIDDLE2". This low value of V_p/V_s ratio likely reflects over-pressurized pores filled with water and CO_2 in the fault zone (Lin, 2019; Lin et al., 2022). This patch, with a spatial extent of 4 km, seems to disappear after the Mw 7.1 mainshock (Figure 3c), suggesting a fault environment change caused by the mainshock. Abundant aftershocks over the 2 months illuminate the entire Ridgecrest fault system, which is characterized by a homogeneous distribution of V_p/V_s ratios with a nominal value of 1.72. The homogeneous distribution as well as the values of the V_p/V_s ratios align closely with those obtained from the complete earthquake data set because aftershocks of the Mw 7.1 mainshock dominate the data set.

We interpret the low V_p/V_s ratio of 1.45 near the Mw 7.1 mainshock's hypocenter between the Mw 5.4 foreshock and the mainshock suggests as evidence of the region enriched with fluids including both water and CO_2 prior to the rupture of the mainshock. The fluid might have been trapped in ellipsoidal pockets, which subsequently escaped through pathways created during the mainshock rupture. These fluid pockets may have caused high pore pressure at the Mw 7.1 hypocenter, thus reducing the effective normal stress and resulting in a locally weak fault (Parsons et al., 2017; Sibson, 1992). This hypothesis aligns with the physics-based rupture simulations that indicate elevated pore fluid pressure is required for nucleating the Ridgecrest earthquakes, and the spatial footprint of the low-V_p/V_s-ratio patch matches the hypothesized rupture nucleation size (Taufiqurrahman et al., 2023). Specifically, neither the static nor the dynamic stress induced by the Mw 6.4 foreshock immediately triggered the mainshock. It is also unclear whether the static stress from the Mw 5.4 foreshock have promoted or inhibited the onset of the Mw 7.1 mainshock (Barnhart et al., 2019; Huang et al., 2020; Jin & Fialko, 2020), and its dynamic stress changes also fail to instantaneously trigger the mainshock (Jin & Fialko, 2020). Such delayed triggering has been observed in other strike-slip earthquake sequences, such as the Landers-Hector Mine pair and the 2023 Turkey earthquake doublet, which could be a reflection of the rate-and-state friction behaviors (Jia et al., 2023; Parsons, 2005; Pollitz & Sacks, 2002; Price & Bürgmann, 2002). In addition, the enclosed fluid inferred from the low V_p/V_s ratios may have provided one necessary weakening mechanism to help nucleate the Mw 7.1 mainshock (Lambert et al., 2021). Once nucleated, this enclosed fluid could further weaken the fault due to thermal pressurization effects (Andrews, 2002; Noda & Lapusta, 2010; Vyas et al., 2023), leading to the observed significant slip near the hypocenter of the Mw 7.1 mainshock (Chen et al., 2020; Goldberg et al., 2020; Wang et al., 2020a).

The earthquakes occurring between the Mw 6.4 foreshock and the Mw 7.1 mainshock did not follow an Omori's law-type decay, indicating that this group of earthquakes might deviate from typical stress-triggered aftershock sequences (Hauksson & Jones, 2020; Ogata & Zhuang, 2006). Foreshocks of other $M > 7$ earthquakes in Southern California have also shown anomalous behavior, suggesting preparatory processes that eventually led to the $M > 7$ mainshocks (Dodge et al., 1995; Yoon et al., 2019). These foreshock sequences bear similarities to earthquake swarms, much like the earthquakes that occurred between the Mw 6.4 and Mw 7.1 events. We also observe changes in the pattern of in situ V_p/V_s ratios from "MIDDLE1" to "MIDDLE2" in the northwest-trending main fault (Figures 3b, 3c, and 4). These changes might indicate that the northeast-trending fault, which ruptured during the Mw 6.4 foreshock, was fluid-rich (Taufiqurrahman et al., 2023); the increase at the fault intersection point reflects a similar process that occurred near the Mw 7.1 hypocenter between "MIDDLE2" and "AFTER." The V_p/V_s ratio increase suggests that there was either fluid movement or aseismic slip within the northwest-trending fault zone around the Mw 5.4 earthquake and between the periods "MIDDLE1" and "MIDDLE2." Given the spatiotemporal scale, this V_p/V_s ratio increase is unlikely due to fluids migrating from the fault intersection to the Mw 7.1 hypocenter for realistic diffusivity of 0.1–1 m^2/s (e.g., Barbour et al., 2017; Chen et al., 2012; Goebel & Brodsky, 2018). However, disconnected, localized fluid movements could possibly cause the observed changes. Alternatively, early afterslip or aseismic slip triggered by the Mw 6.4 earthquake (e.g., Golriz et al., 2021; Huang et al., 2020; Jiang et al., 2021; Premus et al., 2022) could alter the stress conditions in the northwest-trending fault zone and cause the changes in the V_p/V_s ratios. Foreshocks of previous California $M > 7$ earthquakes exhibit lower stress drops and are depleted of high-frequency energy compared to their mainshocks and associated aftershocks (Chen & Shearer, 2013). These features in foreshocks could be indicative of aseismic transients occurring near and prior to the mainshocks (Dodge et al., 1996; Huang et al., 2020). Additionally, they could be attributed to a fluid-rich fault environment or migrating fluid flow, both of which could reduce fault strength and lower differential stress; these processes could also occur concurrently with

aseismic transients. While such foreshocks are not consistently observed before mainshocks (van den Ende & Ampuero, 2020), the transient change in V_p/V_s ratio near the Mw 7.1 mainshock may reflect an underlying fault zone condition that could facilitate the nucleation of other $M > 7$ earthquakes in California and beyond.

5. Conclusions

We apply a high-resolution method to estimate in situ V_p/V_s ratios for similar earthquake clusters during the 2019 Ridgecrest seismic sequence. The majority of the rupture zone is governed by relatively homogeneous V_p/V_s ratios. Slightly low values are resolved in the ALFZ, at the terminus of the LLFZ and the intersection with the GF. Fine-scale V_p/V_s anomalies are revealed near the source regions of the Mw 6.4, 5.4, and 7.1 shocks, with low value before and high one after the mainshock, indicating a fluid rich fault zone environment prior to the earthquake nucleation process, which is likely altered by the mainshock after its rupture.

Data Availability Statement

Data - The original seismic data used in this study were obtained from the Southern California Earthquake Data Center (SCEDC, 2013). The seismic velocity model, location catalog and waveform data used in the V_p/V_s ratio estimation are available through the published work (Lin, 2020; Zhang & Lin, 2014). Software - Figures were made using the public domain GMT software (Wessel et al., 2013) and MATLAB (The MathWorks Inc, 2023).

Acknowledgments
We thank Alice Gabriel and Roland Bürgmann for insightful discussions. We are grateful to Eric Dunham and an anonymous reviewer for their constructive reviews. This research was supported by NSF grants EAR-2022429 (GL) and EAR-2022441 (WF).

References

Abercrombie, R. E., & Mori, J. (1996). Occurrence patterns of foreshocks to large earthquakes in the western United States. *Nature*, *381*(6580), 303–307. https://doi.org/10.1038/381303a0

Adam, L., & Otheim, T. (2013). Elastic laboratory measurements and modeling of saturated basalts. *Journal of Geophysical Research*, *118*(3), 840–851. https://doi.org/10.1002/jgrb.50090

Andrews, D. J. (2002). A fault constitutive relation accounting for thermal pressurization of pore fluid. *Journal of Geophysical Research*, *107*(B12), ESE–15. https://doi.org/10.1029/2002jb001942

Barbour, A. J., Norbeck, J. H., & Rubinstein, J. L. (2017). The effects of varying injection rates in Osage county, Oklahoma, on the 2016 m w 5.8 Pawnee earthquake. *Seismological Research Letters*, *88*(4), 1040–1053. https://doi.org/10.1785/0220170003

Barnhart, W. D., Hayes, G. P., & Gold, R. D. (2019). The July 2019 ridgecrest, California, earthquake sequence: Kinematics of slip and stressing in cross-fault ruptures. *Geophysical Research Letters*, *46*(21), 11859–11867. https://doi.org/10.1029/2019gl084741

Brantut, N., & David, E. C. (2019). Influence of fluids on vp/vs ratio: Increase or decrease? *Geophysical Journal International*, *216*(3), 2037–2043. https://doi.org/10.1093/gji/ggy518

Chen, K., Avouac, J.-P., Aati, S., Milliner, C., Zheng, F., & Shi, C. (2020). Cascading and pulse-like ruptures during the 2019 Ridgecrest earthquakes in the Eastern California Shear Zone. *Nature Communications*, *11*(1), 22. https://doi.org/10.1038/s41467-019-13750-w

Chen, X., Shearer, P., & Abercrombie, R. (2012). Spatial migration of earthquakes within seismic clusters in southern California: Evidence for fluid diffusion. *Journal of Geophysical Research*, *117*(B4). https://doi.org/10.1029/2011jb008973

Chen, X., & Shearer, P. M. (2013). California foreshock sequences suggest aseismic triggering process. *Geophysical Research Letters*, *40*(11), 2602–2607. https://doi.org/10.1002/grl.50444

Christensen, N. I. (1996). Poisson's ratio and crustal seismology. *Journal of Geophysical Research*, *101*(B2), 3139–3156. https://doi.org/10.1029/95jb03446

Dodge, D. A., Beroza, G. C., & Ellsworth, W. L. (1995). Foreshock sequence of the 1992 Landers, California, earthquake and its implications for earthquake nucleation. *Journal of Geophysical Research*, *100*(B6), 9865–9880. https://doi.org/10.1029/95jb00871

Dodge, D. A., Beroza, G. C., & Ellsworth, W. L. (1996). Detailed observations of California foreshock sequences: Implications for the earthquake initiation process. *Journal of Geophysical Research*, *101*(B10), 22371–22392. https://doi.org/10.1029/96jb02269

Dokka, R. K., & Travis, C. J. (1990). Role of the eastern California shear zone in accommodating pacific-north American plate motion. *Geophysical Research Letters*, *17*(9), 1323–1326. https://doi.org/10.1029/gl017i009p01323

Efron, B., & Gong, G. (1983). A leisurely look at the bootstrap, the jackknife and cross-validation. *The American Statistician*, *37*(1), 36–48. https://doi.org/10.2307/2685844

Efron, B., & Tibshirani, R. (1991). Statistical data analysis in the computer age. *Science*, *253*(5018), 390–395. https://doi.org/10.1126/science.253.5018.390

Ellsworth, W. L., & Beroza, G. (1995). Seismic evidence for an earthquake nucleation phase. *Science*, *268*(5212), 851–855. https://doi.org/10.1126/science.268.5212.851

Fialko, Y. (2021). Estimation of absolute stress in the hypocentral region of the 2019 ridgecrest, California, earthquakes. *Journal of Geophysical Research*, *126*(7), e2021JB022000. https://doi.org/10.1029/2021jb022000

Fialko, Y., & Jin, Z. (2021). Simple shear origin of the cross-faults ruptured in the 2019 Ridgecrest earthquake sequence. *Nature Geoscience*, *14*(7), 513–518. https://doi.org/10.1038/s41561-021-00758-5

Goebel, T. H., & Brodsky, E. E. (2018). The spatial footprint of injection wells in a global compilation of induced earthquake sequences. *Science*, *361*(6405), 899–904. https://doi.org/10.1126/science.aat5449

Goldberg, D. E., Melgar, D., Sahakian, V. J., Thomas, A. M., Xu, X., Crowell, B. W., & Geng, J. (2020). Complex rupture of an immature fault zone: A simultaneous kinematic model of the 2019 Ridgecrest, CA earthquakes. *Geophysical Research Letters*, *47*(3), e2019GL086382. https://doi.org/10.1029/2019gl086382

Golriz, D., Bock, Y., & Xu, X. (2021). Defining the coseismic phase of the crustal deformation cycle with seismogeodesy. *Journal of Geophysical Research*, *126*(10), e2021JB022002. https://doi.org/10.1029/2021jb022002

Gong, J., & Fan, W. (2022). Seismicity, fault architecture, and slip mode of the westernmost Gofar transform fault. *Journal of Geophysical Research: Solid Earth*, *127*(11), e2022JB024918. https://doi.org/10.1029/2022jb024918
Hauksson, E., & Jones, L. M. (2020b). Seismicity, stress state, and style of faulting of the Ridgecrest-Coso region from the 1930s to 2019: Seismotectonics of an evolving plate boundary segment. *Bulletin of the Seismological Society of America*, *110*(4), 1457–1473. https://doi.org/10.1785/0120200051
Huang, H., Meng, L., Bürgmann, R., Wang, W., & Wang, K. (2020). Spatio-temporal foreshock evolution of the 2019 M 6.4 and M 7.1 Ridgecrest, California earthquakes. *Earth and Planetary Science Letters*, *551*, 116582. https://doi.org/10.1016/j.epsl.2020.116582
Ide, S. (2019). Frequent observations of identical onsets of large and small earthquakes. *Nature*, *573*(7772), 112–116. https://doi.org/10.1038/s41586-019-1508-5
Jia, Z., Jin, Z., Marchandon, M., Ulrich, T., Gabriel, A.-A., Fan, W., et al. (2023). The complex dynamics of the 2023 Kahramanmaraş, Turkey, m w 7.8-7.7 earthquake doublet. *Science*, *381*(6661), 985–990. https://doi.org/10.1126/science.adi0685
Jia, Z., Wang, X., & Zhan, Z. (2020). Multifault models of the 2019 Ridgecrest sequence highlight complementary slip and fault junction instability. *Geophysical Research Letters*, *47*(17), e2020GL089802. https://doi.org/10.1029/2020gl089802
Jiang, J., Bock, Y., & Klein, E. (2021). Coevolving early afterslip and aftershock signatures of a San Andreas fault rupture. *Science Advances*, *7*(15), eabc1606. https://doi.org/10.1126/sciadv.abc1606
Jin, Z., & Fialko, Y. (2020). Finite slip models of the 2019 Ridgecrest earthquake sequence constrained by space geodetic data and aftershock locations. *Bulletin of the Seismological Society of America*, *110*(4), 1660–1679. https://doi.org/10.1785/0120200060
Kato, A., Obara, K., Igarashi, T., Tsuruoka, H., Nakagawa, S., & Hirata, N. (2012). Propagation of slow slip leading up to the 2011 Mw 9.0 Tohoku-Oki earthquake. *Science*, *335*(6069), 705–708. https://doi.org/10.1126/science.1215141
Kirschvink, J. L. (1980). The least-squares line and plane and the analysis of palaeomagnetic data. *Geophysical Journal of the Royal Astronomical Society*, *62*(3), 699–718. https://doi.org/10.1111/j.1365-246x.1980.tb02601.x
Kohli, A., Wolfson-Schwehr, M., Prigent, C., & Warren, J. M. (2021). Oceanic transform fault seismicity and slip mode influenced by seawater infiltration. *Nature Geoscience*, *14*(8), 606–611. https://doi.org/10.1038/s41561-021-00778-1
Kuster, G. T., & Toksöz, M. N. (1974). Velocity and attenuation of seismic waves in two-phase media: Part I. Theoretical formulations. *Geophysics*, *39*(5), 587–606. https://doi.org/10.1190/1.1440450
Lambert, V., Lapusta, N., & Faulkner, D. (2021). Scale dependence of earthquake rupture prestress in models with enhanced weakening: Implications for event statistics and inferences of fault stress. *Journal of Geophysical Research*, *126*(10), e2021JB021886. https://doi.org/10.1029/2021jb021886
Lemmon, E. W., Bell, I. H., Huber, M. L., & McLinden, M. O. (2023). Thermophysical properties of fluid systems. In P. J. Linstrom & W. G. Mallard (Eds.), *NIST chemistry WebBook, NIST standard reference database* (Vol. 69). National Institute of Standards and Technology.
Lin, G. (2018). The source-specific station term and waveform cross-correlation earthquake location package and its applications to California and New Zealand. *Seismological Research Letters*, *89*(5), 1877–1885. https://doi.org/10.1785/0220180108
Lin, G. (2019). Spatiotemporal variations of in situ Vp/Vs ratio within the Salton Sea Geothermal Field, southern California. *Geothermics*, *84*, 101740. https://doi.org/10.1016/j.geothermics.2019.101740
Lin, G. (2020). Waveform cross-correlation relocation and focal mechanisms for the 2019 Ridgecrest earthquake sequence [Dataset]. *Seismological Research Letters*, *91*(4), 2055–2061. https://doi.org/10.1785/0220190277
Lin, G., Huerfano, V. A., & Fan, W. (2021). Crustal architecture of Puerto Rico using body-wave seismic tomography and high-resolution earthquake relocation. *Seismological Research Letters*, *93*(2A), 555–566. https://doi.org/10.1785/0220210223
Lin, G., Peng, Z., & Neves, M. (2022). Comparisons of in situ Vp/Vs ratios and seismic characteristics between northern and southern California. *Geophysical Journal International*, *229*(3), 2162–2174. https://doi.org/10.1093/gji/ggac038
Lin, G., & Shearer, P. M. (2006). The COMPLOC earthquake location package. *Seismological Research Letters*, *77*(4), 440–444. https://doi.org/10.1785/gssrl.77.4.440
Lin, G., & Shearer, P. M. (2007). Estimating local Vp/Vs ratios within similar earthquake clusters. *Bulletin of the Seismological Society of America*, *97*(2), 379–388. https://doi.org/10.1785/0120060115
Lin, G., & Shearer, P. M. (2009). Evidence for water-filled cracks in earthquake source regions. *Geophysical Research Letters*, *36*(L17315). https://doi.org/10.1029/2009gl039098
Lin, G., Shearer, P. M., Hauksson, E., & Thurber, C. H. (2007). A three-dimensional crustal seismic velocity model for southern California from a composite event method. *Journal of Geophysical Research*, *112*(B11306). https://doi.org/10.1029/2007jb004977
Lin, G., Shearer, P. M., Matoza, R. S., Okubo, P. G., & Amelung, F. (2014). Three-dimensional seismic velocity structure of Mauna Loa and Kilauea volcanoes in Hawaii from local seismic tomography. *Journal of Geophysical Research*, *119*(5), 4377–4392. https://doi.org/10.1002/2013jb010820
Lin, G., Thurber, C. H., Zhang, H., Hauksson, E., Shearer, P. M., Waldhauser, F., et al. (2010). A California statewide three-dimensional seismic velocity model from both absolute and differential times. *Bulletin of the Seismological Society of America*, *100*(1), 225–240. https://doi.org/10.1785/0120090028
Liu, T., Gong, J., Fan, W., & Lin, G. (2023). In-situ Vp/Vs reveals fault-zone material variation at the westernmost Gofar Transform Fault, East Pacific Rise. *Journal of Geophysical Research*, *128*(3), e2022JB025310. https://doi.org/10.1029/2022jb025310
Lozos, J. C., & Harris, R. A. (2020). Dynamic rupture simulations of the m6. 4 and m7. 1 July 2019 ridgecrest, California, earthquakes. *Geophysical Research Letters*, *47*(7), e2019GL086020. https://doi.org/10.1029/2019gl086020
McGuire, J. J., Collins, J. A., Gouédard, P., Roland, E., Lizarralde, D., Boettcher, M. S., et al. (2012). Variations in earthquake rupture properties along the Gofar transform fault, east pacific rise. *Nature Geoscience*, *5*(5), 336–341. https://doi.org/10.1038/ngeo1454
McLaskey, G. C. (2019). Earthquake initiation from laboratory observations and implications for foreshocks. *Journal of Geophysical Research*, *124*(12), 12882–12904. https://doi.org/10.1029/2019jb018363
Meng, H., & Fan, W. (2021). Immediate foreshocks indicating cascading rupture developments for 527 M 0.9 to 5.4 Ridgecrest earthquakes. *Geophysical Research Letters*, *48*(19), e2021GL095704. https://doi.org/10.1029/2021gl095704
Michelini, A., & Bolt, B. A. (1986). Application of the principal parameters method to the 1983 Coalinga, California, aftershock sequence. *Bulletin of the Seismological Society of America*, *76*(2), 409–420. https://doi.org/10.1785/bssa0760020409
Milliner, C., Aati, S., & Avouac, J.-P. (2022). Fault friction derived from fault bend influence on coseismic slip during the 2019 Ridgecrest mw 7.1 mainshock. *Journal of Geophysical Research*, *127*(11), e2022JB024519. https://doi.org/10.1029/2022jb024519
Noda, H., & Lapusta, N. (2010). Three-dimensional earthquake sequence simulations with evolving temperature and pore pressure due to shear heating: Effect of heterogeneous hydraulic diffusivity. *Journal of Geophysical Research*, *115*(B12). https://doi.org/10.1029/2010jb007780
O'Connell, R. J., & Budiansky, B. (1974). Seismic velocities in dry and saturated cracked solids. *Journal of Geophysical Research*, *79*(35), 5412–5426. https://doi.org/10.1029/jb079i035p05412

Ogata, Y., & Zhuang, J. (2006). Space–time etas models and an improved extension. *Tectonophysics*, *413*(1–2), 13–23. https://doi.org/10.1016/j.tecto.2005.10.016

Parsons, T. (2005). A hypothesis for delayed dynamic earthquake triggering. *Geophysical Research Letters*, *32*(4). https://doi.org/10.1029/2004gl021811

Parsons, T., Malagnini, L., & Akinci, A. (2017). Nucleation speed limit on remote fluid-induced earthquakes. *Science Advances*, *3*(8), e1700660. https://doi.org/10.1126/sciadv.1700660

Pollitz, F. F., & Sacks, I. S. (2002). Stress triggering of the 1999 hector mine earthquake by transient deformation following the 1992 landers earthquake. *Bulletin of the Seismological Society of America*, *92*(4), 1487–1496. https://doi.org/10.1785/0120000918

Ponti, D. J., Blair, J. L., Rosa, C. M., Thomas, K., Pickering, A. J., Akciz, S., et al. (2020). Documentation of surface fault rupture and ground-deformation features produced by the 4 and 5 July 2019 mw 6.4 and mw 7.1 Ridgecrest earthquake sequence. *Seismological Research Letters*, *91*(5), 2942–2959. https://doi.org/10.1785/0220190322

Premus, J., Gallovič, F., & Ampuero, J.-P. (2022). Bridging time scales of faulting: From coseismic to postseismic slip of the m w 6.0 2014 south Napa, California earthquake. *Science Advances*, *8*(38), eabq2536. https://doi.org/10.1126/sciadv.abq2536

Price, E. J., & Bürgmann, R. (2002). Interactions between the landers and hector mine, California, earthquakes from space geodesy, boundary element modeling, and time-dependent friction. *Bulletin of the Seismological Society of America*, *92*(4), 1450–1469. https://doi.org/10.1785/0120000924

Qiu, H., Ben-Zion, Y., Catchings, R., Goldman, M. R., Allam, A. A., & Steidl, J. (2021). Seismic imaging of the Mw 7.1 Ridgecrest earthquake rupture zone from data recorded by dense linear arrays. *Journal of Geophysical Research*, *126*(7), e2021JB022043. https://doi.org/10.1029/2021jb022043

Renard, F., Cordonnier, B., Kobchenko, M., Kandula, N., Weiss, J., & Zhu, W. (2017). Microscale characterization of rupture nucleation unravels precursors to faulting in rocks. *Earth and Planetary Science Letters*, *476*, 69–78. https://doi.org/10.1016/j.epsl.2017.08.002

Renard, F., Weiss, J., Mathiesen, J., Ben-Zion, Y., Kandula, N., & Cordonnier, B. (2018). Critical evolution of damage toward system-size failure in crystalline rock. *Journal of Geophysical Research*, *123*(2), 1969–1986. https://doi.org/10.1002/2017jb014964

Roland, E., Lizarralde, D., McGuire, J. J., & Collins, J. A. (2012). Seismic velocity constraints on the material properties that control earthquake behavior at the Quebrada-Discovery-Gofar transform faults, east pacific rise. *Journal of Geophysical Research*, *117*(B11). https://doi.org/10.1029/2012jb009422

Ross, Z. E., Idini, B., Jia, Z., Stephenson, O. L., Zhong, M., Wang, X., et al. (2019). Hierarchical interlocked orthogonal faulting in the 2019 Ridgecrest earthquake sequence. *Science*, *366*(6463), 346–351. https://doi.org/10.1126/science.aaz0109

Ruiz, S., Metois, M., Fuenzalida, A., Ruiz, J., Leyton, F., Grandin, R., et al. (2014). Intense foreshocks and a slow slip event preceded the 2014 Iquique Mw 8.1 earthquake. *Science*, *345*(6201), 1165–1169. https://doi.org/10.1126/science.1256074

SCEDC. (2013). Southern California Earthquake Center, Caltech [Dataset]. https://doi.org/10.7909/C3WD3xH1

Shearer, P. M., Hardebeck, J. L., Astiz, L., & Richards-Dinger, K. B. (2003). Analysis of similar event clusters in aftershocks of the 1994 Northridge, California, earthquake. *Journal of Geophysical Research*, *108*(B1), B1–B2035. https://doi.org/10.1029/2001JB000685

Shelly, D. R. (2020). A high-resolution seismic catalog for the initial 2019 Ridgecrest earthquake sequence: Foreshocks, aftershocks, and faulting complexity. *Seismological Research Letters*, *91*(4), 1971–1978. https://doi.org/10.1785/0220190309

Sibson, R. (1992). Implications of fault-valve behaviour for rupture nucleation and recurrence. *Tectonophysics*, *211*(1–4), 283–293. https://doi.org/10.1016/0040-1951(92)90065-e

Takei, Y. (2002). Effect of pore geometry on Vp/Vs: From equilibrium geometry to crack. *Journal of Geophysical Research*, *107*(B2), 2043. https://doi.org/10.1029/2001jb000522

Taufiqurrahman, T., Gabriel, A.-A., Li, D., Ulrich, T., Li, B., Carena, S., et al. (2023). Dynamics, interactions and delays of the 2019 Ridgecrest rupture sequence. *Nature*, *618*(7964), 308–315. https://doi.org/10.1038/s41586-023-05985-x

The MathWorks Inc. (2023). MATLAB version: 9.14.0 (R2023a). The MathWorks Inc. [Software]. Retrieved from https://www.mathworks.com/

Thompson Jobe, J. A., Philibosian, B., Chupik, C., Dawson, T., K. Bennett, S. E., Gold, R., et al. (2020). Evidence of previous faulting along the 2019 Ridgecrest, California, earthquake ruptures. *Bulletin of the Seismological Society of America*, *110*(4), 1427–1456. https://doi.org/10.1785/0120200041

Tong, P., Yao, J., Liu, Q., Li, T., Wang, K., Liu, S., et al. (2021). Crustal rotation and fluids: Factors for the 2019 Ridgecrest earthquake sequence? *Geophysical Research Letters*, *48*(3), e2020GL090853. https://doi.org/10.1029/2020gl090853

Trugman, D. T., Ross, Z. E., & Johnson, P. A. (2020). Imaging stress and faulting complexity through earthquake waveform similarity. *Geophysical Research Letters*, *47*(1), e2019GL085888. https://doi.org/10.1029/2019gl085888

van den Ende, M. P., & Ampuero, J.-P. (2020). On the statistical significance of foreshock sequences in southern California. *Geophysical Research Letters*, *47*(3), e2019GL086224. https://doi.org/10.1029/2019gl086224

Vyas, J. C., Gabriel, A., Ulrich, T., Mai, P. M., & Ampuero, J. (2023). How does thermal pressurization of pore fluids affect 3D strike-slip earthquake dynamics and ground motions? *Bulletin of the Seismological Society of America*, *113*(5), 1992–2008. https://doi.org/10.1785/0120220205

Walsh, J. B. (1969). New analysis of attenuation in partially melted rock. *Journal of Geophysical Research*, *74*(17), 4333–4337. https://doi.org/10.1029/jb074i017p04333

Wang, K., Dreger, D. S., Tinti, E., Bürgmann, R., & Taira, T. (2020a). Rupture process of the 2019 Ridgecrest, California Mw 6.4 foreshock and Mw 7.1 earthquake constrained by seismic and geodetic data. *Bulletin of the Seismological Society of America*, *110*(4), 1603–1626. https://doi.org/10.1785/0120200108

Wang, K., Dreger, D. S., Tinti, E., Bürgmann, R., & Taira, T. (2020b). Rupture process of the 2019 Ridgecrest, California m w 6.4 foreshock and m w 7.1 earthquake constrained by seismic and geodetic data. *Bulletin of the Seismological Society of America*, *110*(4), 1603–1626. https://doi.org/10.1785/0120200108

Wessel, P., Smith, W. H. F., Scharroo, R., Luis, J., & Wobbe, F. (2013). Generic mapping tools: Improved version released [Software]. *Eos, Transactions American Geophysical Union*, *94*(45), 409–410. https://doi.org/10.1002/2013eo450001

White, M. C., Fang, H., Catchings, R. D., Goldman, M. R., Steidl, J. H., & Ben-Zion, Y. (2021). Detailed traveltime tomography and seismic catalogue around the 2019 m w7. 1 Ridgecrest, California, earthquake using dense rapid-response seismic data. *Geophysical Journal International*, *227*(1), 204–227. https://doi.org/10.1093/gji/ggab224

Wibberley, C. A., Yielding, G., & Di Toro, G. (2008). Recent advances in the understanding of fault zone internal structure: A review. *Geological Society, London, Special Publications*, *299*(1), 5–33. https://doi.org/10.1144/sp299.2

Yang, Z., Zhao, D., Cheng, B., & Dong, Y. (2022). Structural control on the 2019 Ridgecrest earthquake from local seismic tomography. *Physics of the Earth and Planetary Interiors*, *324*, 106853. https://doi.org/10.1016/j.pepi.2022.106853

Yoon, C. E., Yoshimitsu, N., Ellsworth, W. L., & Beroza, G. C. (2019). Foreshocks and mainshock nucleation of the 1999 m w 7.1 hector mine, California, earthquake. *Journal of Geophysical Research*, *124*(2), 1569–1582. https://doi.org/10.1029/2018jb016383

Zhang, Q., & Lin, G. (2014). Three-dimensional Vp and Vp/Vs models in the Coso geothermal area, California: Seismic characterization of the magmatic system. [Dataset]. *Journal of Geophysical Research*, *119*(6), 4907–4922. https://doi.org/10.1002/2014jb010992

Zhu, W., Allison, K. L., Dunham, E. M., & Yang, Y. (2020). Fault valving and pore pressure evolution in simulations of earthquake sequences and aseismic slip. *Nature Communications*, *11*(1), 4833. https://doi.org/10.1038/s41467-020-18598-z

Zimmerman, R. W. (1984). Elastic moduli of a solid with spherical pores: New self-consistent method. *International Journal of Rock Mechanics and Mining Sciences & Geomechanics Abstracts*, *21*(6), 339–343. https://doi.org/10.1016/0148-9062(84)90366-8